

# Large Eddy Simulation of Evolution of a Passive Scalar in Plane Jet

C. Le Ribault\*

*Laboratoire de Mécanique des Fluides et d'Acoustique, 69131 Ecully Cedex, France*

S. Sarkar†

*University of California, San Diego, La Jolla, California 92093-0411*

and

S. A. Stanley‡

*Lawrence Berkeley National Laboratory, Berkeley, California 94720*

Large-eddy simulation (LES) is performed to investigate the passive scalar development in a plane jet. This is a follow-up of our previous simulation of the jet flowfield. The LES results are compared to both experiments and direct numerical simulation (DNS). Two subgrid models are investigated: the dynamic Smagorinsky model and the dynamic mixed model. It is found that the evolution of mean scalar and turbulent scalar intensity is well represented. Some properties of the LES models such as the evolution of the dynamic constant and the subgrid viscosity are also discussed. Profiles of higher scalar moments show non-Gaussianity near the jet boundaries that is associated with external intermittency. Finally, the probability density function (PDF) of the passive scalar computed with LES is obtained and compared with the true PDF obtained with DNS. The LES approach is found able to represent the main characteristics of the PDF including qualitative changes during its initial evolution.

## I. Introduction

TRANSPORT and mixing of a scalar is very important for engineering and environmental problems such as fuel-oxidant mixing and contaminant dispersion. A necessary prerequisite for prediction of the two-phase mixing that occurs in the establishment of a premixed reactant mixture is to compute the limiting case of passive scalar transport.

Several experiments of heated plane jets exist where the temperature difference with respect to the ambient, kept small to limit buoyancy effects, can be considered as a passive scalar.<sup>1-4</sup> Jenkins and Goldschmidt<sup>1</sup> measured temperature, shear stress, and velocity-temperature correlation in the fully turbulent region of a plane jet. Davies et al.<sup>2</sup> performed measurements to investigate why the mean temperature distribution is wider than that of the velocity. Browne et al.<sup>3</sup> provided measurements in the initial region of the jet. Ramaprian and Chandrasekhara<sup>4</sup> performed a study using Doppler anemometry in the fully developed region.

Large-eddy simulation (LES) is a promising approach to the problem of predicting the flow and associated scalar transport. Recent reviews of different LES approaches include those by Lesieur and Metais<sup>5</sup> and Moin.<sup>6</sup> LES of passive scalar has mostly relied on a simple gradient approximation to the subgrid scalar flux that introduces a turbulent Prandtl number  $Pr_r$ . The value of Prandtl number  $Pr_r$  is either a specified model parameter<sup>7</sup> or obtained using a dynamic procedure.<sup>8</sup> The dynamic Prandtl number model has been used, for example, by Akselvoll and Moin<sup>9</sup> as part of the computation of two coaxial jets with fast combustion and by Vreman et al.<sup>10</sup> for closure of the energy equation in an application to a temporally evolving compressible mixing layer. An alternate procedure for obtaining the subgrid scalar flux introduces a tensor eddy diffusivity that is given by modeled stretched-vortex dynamics.<sup>11</sup> LES of nonpremixed turbulent reacting flows often require models for the subgrid scalar variance in addition to a prediction of the filtered scalar. Proposals for modeling the subgrid scalar variance include a scale-similarity

model,<sup>12</sup> a gradient model,<sup>13</sup> and a model based on moment-based reconstruction of the scalar field.<sup>14</sup>

Direct simulation is a very accurate numerical method for flow prediction but requires very refined meshes and is limited to moderate Reynolds number. A direct simulation of a plane jet has been performed,<sup>15</sup> and the evolution of the mean and fluctuating passive scalar and its probability density functions have been studied. An LES of the same (as well as higher-Reynolds-number) plane jet but without the passive scalar has also been performed.<sup>16</sup> In this LES study,<sup>16</sup> the flowfield was studied in detail and the results compared with experiments and direct numerical simulation (DNS). In the current work, we extend the study to scalar transport in the plane jet.

The goal of the present paper is to test subgrid models for the passive scalar and to investigate, by comparison with the direct simulation and experiments, if LES is able to predict the evolution of passive scalar statistics including its probability density function.

## II. Governing Equations

For brevity, we do not repeat the equations for the filtered momentum equations and models for the subgrid stress tensor,  $\tau_{ij} = \widetilde{u_i u_j} - \widetilde{u_i} \widetilde{u_j}$ , which were described in detail previously.<sup>16</sup>

### A. Passive Scalar Equation

The flow is governed by the Navier-Stokes equations, representing mass conservation, momentum conservation, and energy conservation. The Navier-Stokes equations are solved in their compressible form, for future generalization to high-speed flow, but in the case studied here, the Mach number is sufficiently small so that compressibility effects can be neglected.

The dimensional scalar transport equation (for example, see Libby and Williams<sup>17</sup>) can be written as

$$\frac{\partial}{\partial t^*}(\rho^* \xi^*) + \frac{\partial}{\partial x_k^*}(\rho^* u_k^* \xi^*) = \frac{\partial}{\partial x_k^*} \left( \rho^* D^* \frac{\partial \xi^*}{\partial x_k^*} \right) \quad (1)$$

This equation is nondimensionalized using the reference values  $\rho_r^*$ ,  $D_r^*$ , and  $l_r^*$  to give

$$\frac{\partial}{\partial t}(\rho \xi) + \frac{\partial}{\partial x_k}(\rho u_k \xi) = \frac{D_r^*}{l_r^* u_r^*} \frac{\partial}{\partial x_k} \left( \rho D \frac{\partial \xi}{\partial x_k} \right) \quad (2)$$

The parameters  $Re_r = u_r^* l_r^* / \nu_r^*$  and  $Sc_r = \nu_r^* / D_r^*$  are, respectively, the reference values of the Reynolds number and the Schmidt

Received 22 April 2000; revision received 26 December 2000; accepted for publication 26 January 2001. Copyright © 2001 by the American Institute of Aeronautics and Astronautics, Inc. All rights reserved.

\*Staff Scientist.

†Professor, Mechanical and Aerospace Engineering. Member AIAA.

‡Postdoctoral Fellow, Center for Computational Science and Engineering, Member AIAA.

number. Because the simulations are performed for constant scalar diffusivity  $D = D^*/D_r^* = 1$ , the equation of the passive scalar can be written as

$$\frac{\partial \rho \xi}{\partial t} + \frac{\partial}{\partial x_k} (\rho u_k \xi) = \frac{1}{Re_r Sc_r} \frac{\partial}{\partial x_k} \left( \rho \frac{\partial \xi}{\partial x_k} \right) \quad (3)$$

### B. Filtered Scalar Equation

The Navier–Stokes equations are filtered using a top-hat filter. A filter width  $\Delta = 2h$ , where  $h$  represents the grid spacing, is used. In our previous study<sup>16</sup> the influence of filter size was studied, and the choice,  $\Delta = 2h$ , which was found to give the best results, is retained for the current study. Filtering of the passive scalar equation leads to

$$\frac{\partial \bar{\rho} \tilde{\xi}}{\partial t} + \frac{\partial}{\partial x_k} \bar{\rho} \tilde{u}_k \tilde{\xi} = \frac{1}{Re_r Sc_r} \frac{\partial}{\partial x_k} \left( \bar{\rho} \frac{\partial \tilde{\xi}}{\partial x_k} \right) - \frac{\partial \bar{\rho} q_k^\xi}{\partial x_k} \quad (4)$$

where  $q_k^\xi$  is the subgrid scalar flux,

$$q_k^\xi = \widetilde{u_k \xi} - \tilde{u}_k \tilde{\xi} \quad (5)$$

### C. Subgrid Models

The standard subgrid models, developed for the velocity field, can also be applied to the passive scalar equation. The dynamic Smagorinsky model applied to both scalar and momentum transport, as well as the dynamic mixed model again applied to both scalar and momentum transport are investigated here. These models are introduced into the scalar equation similarly to the momentum equation.

#### Dynamic Smagorinsky Model

The more classical model is the Smagorinsky model,<sup>18</sup> which, for a passive scalar, can be written as

$$q_k^\xi = -\alpha_r \frac{\partial \tilde{\xi}}{\partial x_k} \quad \text{with} \quad \alpha_r = C_\xi^2 \Delta^2 |\bar{S}|, \quad |\bar{S}|^2 = \frac{1}{2} S_{pq} S_{pq} \quad (6)$$

In the standard model,  $C_\xi$  has a value slightly higher than  $C_s$ , the analogous constant for subgrid momentum transport;  $C_\xi/C_s \approx 1.4$  (Ref. 7).

The dynamic version<sup>19</sup> has been shown to be much more accurate than the standard version for predicting the velocity field in the plane jet.<sup>16</sup> Therefore, a dynamic procedure is also used for the passive scalar. The square of the constant  $C_\xi^2$  is replaced by a coefficient  $C_{d\xi}$ , which is dynamically computed and depends on the local structure of the flow. The Smagorinsky eddy diffusivity formulation is retained:

$$q_k^\xi = -C_{d\xi} \Delta^2 |\bar{S}| \frac{\partial \tilde{\xi}}{\partial x_k} \quad (7)$$

To compute  $C_{d\xi}$ , a test filter, denoted by a caret and corresponding to a filter width larger than that of the LES, is introduced. The consecutive  $\Delta$  application of these two filters defines a filter with a filter width of  $\kappa \Delta$ . The dynamic constant is calculated with a least-squares approach according to

$$C_{d\xi} = \langle M_i L_i \rangle / \langle M_i M_i \rangle \quad (8)$$

$$L_i = \widehat{\widehat{u_i \xi}} - \widehat{\widehat{u_i}} \widehat{\widehat{\xi}} \quad (9)$$

$$M_i = -(\kappa \Delta)^2 |\widehat{\widehat{S}}| \widehat{\widehat{\xi}} + \Delta^2 |\widehat{\widehat{S}}| \widehat{\widehat{\xi}} \quad (10)$$

To prevent numerical instability caused by negative values of  $C_{d\xi}$ , the numerator and denominator are averaged in the homogeneous direction. The constant  $C_{d\xi}$  is artificially set to zero during the few instances when it is still negative.

#### Dynamic Mixed Model

Similar to the mixed model for the subgrid momentum flux, the mixed model for the subgrid scalar flux,

$$q_k^\xi = -C_{d\xi} \Delta^2 |\bar{S}| \frac{\partial \tilde{\xi}}{\partial x_k} + \overline{\widetilde{u_k \xi}} - \overline{\tilde{u}_k \tilde{\xi}} \quad (11)$$

also consists of a Smagorinsky part and a scale-similarity part. In the dynamic version, the constant of the Smagorinsky part is dynamically computed. This model takes advantage of the correct dissipation produced by the dynamic eddy-viscosity part while the similarity part allows other effects such as the backscatter of energy from subgrid scales to resolved scales and anisotropic energy transfers between grid and subgrid-scale motion.

The dynamic model coefficient is obtained by

$$H_i + C_{d\xi} M_i = L_i \quad (12)$$

where  $M_i$  and  $L_i$  are defined by Eq. (9) and (10), respectively, and  $H_i$  is as follows:

$$H_i = \widehat{\widehat{u_i \xi}} - \widehat{\widehat{u_i}} \widehat{\widehat{\xi}} - \left( \widehat{\widehat{u_i \xi}} - \widehat{\widehat{u_i}} \widehat{\widehat{\xi}} \right) \quad (13)$$

The dynamic model coefficient is obtained with the least-squares approach:

$$C_{d\xi} = \langle M_i (L_i - H_i) \rangle / \langle M_i M_i \rangle \quad (14)$$

## III. Numerical Method and Inflow Conditions

Because the numerical method has already been largely described in our previous work,<sup>15,16</sup> only its principal characteristics are recalled here. For the velocity, spatial derivatives are computed using a nonuniform fourth-order compact scheme based on the uniform scheme of Lele.<sup>20</sup> To ensure long-time nonlinear stability, a fourth-order nonuniform compact filter is applied to the field at each iteration. The fourth-order Runge–Kutta scheme of Carpenter et al.<sup>21</sup> is used for the time integration of the convective terms.

For the passive scalar equation, the flux-corrected transport scheme of Zalesak<sup>22</sup> is used. This scheme is chosen to ensure that the passive scalar remains bounded between its extrema of 0 and 1. A predictor stage is performed with a first-order upwind scheme, which produces a monotone solution. The predicted solution is then modified by a corrector stage using the difference between a fourth-order compact evaluation and the low-order scheme. This correction is nonlinearly limited to avoid spurious numerical oscillations.

For the boundary conditions, at the outflow as well as the upper and lower sidewall boundaries, nonreflecting conditions based on characteristic equations are applicable,<sup>23,24</sup> and that suggested by Thompson<sup>23</sup> is implemented. At the outflow boundary, a pressure relaxation boundary condition is also used.<sup>25</sup> At the inflow boundary, the time variation of the incoming characteristic variables are specified whereas the equation for the outgoing characteristic variable is solved using internal biased derivatives. Moreover, to isolate the interior of the domain from the effects of the boundary conditions, a buffer zone based on the approach of Hu<sup>26</sup> is used at the nonreflecting boundaries.

The longitudinal mean velocity profile at the inflow is a top-hat profile with shear layers at the edges. A hyperbolic tangent profile is used:

$$U = [(U_1 + U_2)/2] + [(U_1 - U_2)/2] \tanh(y/2\theta) \quad (15)$$

where  $\theta$  is the momentum thickness of the shear layer,  $U_1$  is the longitudinal velocity in the middle of the jet, and  $U_2$  is the coflow velocity.

The same hyperbolic tangent profile is used for the passive scalar:

$$\xi = [(\xi_1 + \xi_2)/2] + [(\xi_1 - \xi_2)/2] \tanh(y/2\theta) \quad (16)$$

with  $\xi_1 = 1.0$  and  $\xi_2 = 0.0$  in the jet and coflow, respectively. The value of  $\theta$  used for the passive scalar is the same as that used for the mean longitudinal velocity profile. For the velocity, a broadband forcing representative of isotropic turbulence is utilized at the inflow, and a lateral shape is applied such that the fluctuation intensity peaks in the shear layers on either side of the jet.

## IV. Computational Results

### A. Jet and Grid Parameters

The case discussed here corresponds to the three-dimensional, unsteady simulation of the strong jet simulated previously using DNS.<sup>15</sup> The velocity field of that jet was also simulated subsequently using LES.<sup>16</sup>

The initial jet Reynolds number is  $Re_d = \rho \Delta \bar{U}_j d / \mu = 3 \times 10^3$ , where  $\Delta \bar{U}_j$  is the velocity difference between the two streams at the inflow and  $d$  is the jet slot width. The ratio of the velocity between the low- and high-speed streams is 0.09. The Schmidt number  $Sc = \mu / \rho D_\xi = 1.0$ , and the Prandtl number  $Pr = C_p \mu / k = 0.72$ . The Mach number of the high-speed stream is 0.35, and the convective Mach number of the shear layer is  $M_c = 0.16$ . At such low Mach numbers, the physical characteristics of the flow are similar to those of an incompressible flow, and all of the subgrid models used in the computations are those developed for incompressible flows. The Reynolds number used here is relatively small for a LES but has been chosen to make comparison with DNS. In our previous LES,<sup>16</sup> computations of a jet at the larger Reynolds number of  $3 \times 10^4$  have been performed, but, consistent with experimental data in jets starting with turbulent inflow conditions, no strong differences appear in the results.

A  $61 \times 105 \times 16$  grid is used with the DNS domain size:  $L_x = 12$ ,  $L_y = 15$ , and  $L_z = 4$ , where the jet slot width  $h$  is used for normalization. A slight stretching is used in the  $x$  and  $y$  directions but this stretching has been found to have a very small influence on the solution, as discussed by Le Ribault et al.<sup>16</sup> The LES mesh has approximately a factor of 22 fewer points than the DNS grid. The CPU time of one LES simulation with the dynamic Smagorinsky model on a C90 is approximately of 7 h, whereas that of the DNS is approximately 120 h.

Computations are performed with the dynamic Smagorinsky model and the dynamic mixed model. A computation was attempted on the LES grid without any LES model. This computation was unstable, confirming the necessity of an LES model.

### B. Modeling and Numerical Errors

LES are typically performed on grids that are just fine enough to resolve the important large-scale flow structures, and numerical discretization errors on such grids can have considerable effects on the simulation results. This problem has been recently discussed in the literature, for example, by Vreman,<sup>27</sup> Salvetti and Beaux,<sup>28</sup> and Kravchenko and Moin.<sup>29</sup> The difference between LES and DNS results is the total error, which is the sum of two terms: modeling error arising from the subgrid model and the discretization error caused by the numerical method. A method to separate those two errors has been proposed by Vreman<sup>27</sup> based on the expectation that the discretization error in the LES decreases when the resolution is increased with the filter width kept constant. This method had already been used by Le Ribault et al.<sup>16</sup> to separate the numerical and the modeling error associated with the predicted jet half-width based on the velocity. The same method is now used to separate the two errors in the case of the evolution of the jet half-width based on the passive scalar.

A new LES is performed on a finer grid keeping the same filter width. The computation is performed with the dynamic Smagorinsky model. The grid step is divided by two in the  $x$  and  $z$  directions. The difference between the two LES represents the effects of the numerical error on the jet halfwidth  $\delta_\xi$ :

$$\text{err}_{\text{num}} = \delta_\xi^{\text{LES}} - \delta_\xi^{\text{fine grid LES}} \quad (17)$$

whereas the difference between the fine grid LES and the DNS approximates the modeling error,

$$\text{err}_{\text{mod}} = \delta_\xi^{\text{fine grid LES}} - \delta_\xi^{\text{DNS}} \quad (18)$$

Figure 1 shows the effects of those two errors on the evolution of the jet half-width. Both modeling and discretization errors are relatively small with the dynamic Smagorinsky model. Whereas both errors have approximately the same magnitude, the signs are opposite, which implies that the discretization error assists the subgrid model and that the total error is smaller than the modeling error.

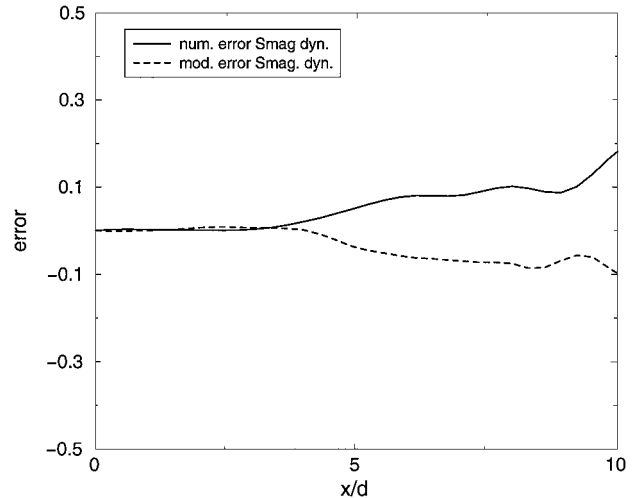


**Fig. 1** Comparison of numerical and modeling errors in the LES prediction of the downstream evolution of jet half-width based on the scalar field; dynamic Smagorinsky model used for both momentum and passive scalar.

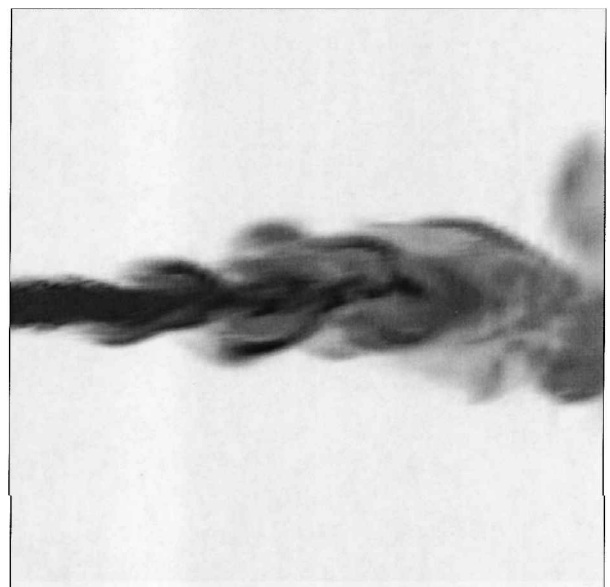


**Fig. 2** Instantaneous passive scalar contours produced by dynamic Smagorinsky model on an  $xy$  plane,  $z = 8$ .

Interestingly, cancellation of modeling and discretization errors has been observed previously in LES of the velocity field, for example, the plane shear layer<sup>10</sup> and the plane jet.<sup>16</sup>

### C. Visualization of the Passive Scalar Field

Isocontours of the passive scalar field obtained by the dynamic Smagorinsky model and by the dynamic mixed model are presented in Figs. 2 and 3, respectively. White contours indicate pure coflow fluid,  $\xi = 0$ , and black indicates pure jet fluid,  $\xi = 1$ . The main characteristics of the passive scalar field are qualitatively captured by both models. In the initial region, the column of pure jet fluid, as well as its slight spreading due to the effects of turbulent diffusion, can be seen. Then regions of white appear in the jet accompanied with dark patches in the freestream, showing the entrainment of coflow fluid by large-scale rollups of the shear layers at the jet edges. Farther downstream, small-scale mixing has reduced the extent of pure jet and coflow fluid, but still small patches of fluid, which are predominantly composed of one fluid type or the other, can be seen. To summarize, the instantaneous large-scale field compares well with DNS, but due to the coarser mesh, there are fewer small-scale features.

**Table 1** Jet growth rates based on the passive scalar and centerline scalar decay rates for current results, DNS results, and several experimental results

Source	$K_{1\xi}$	$K_{2\xi}$	$C_{1\xi}$	$C_{2\xi}$	$K_{1u}/K_{1\xi}$	$C_{1u}/C_{1\xi}$
DNS	0.137	0.072	0.272	-0.38	0.67	0.70
Dynamic Smagorinsky	0.158	-0.63	0.292	-0.75	0.58	0.65
Dynamic mixed	0.128	1.21	0.277	-0.137	0.75	0.72
Ramaprian and Chandrasekhara <sup>4</sup>	0.167	2.00	0.194	6.00	0.66	0.87
Browne et al. <sup>3</sup>	0.128	5.00	0.189	7.86	0.81	0.76
Jenkins and Goldschmidt <sup>1</sup>	0.123	0.090	0.261	-5.62	0.71	0.61
Davies et al. <sup>2</sup>	0.115	2.05	0.258	0.920	0.87	0.61

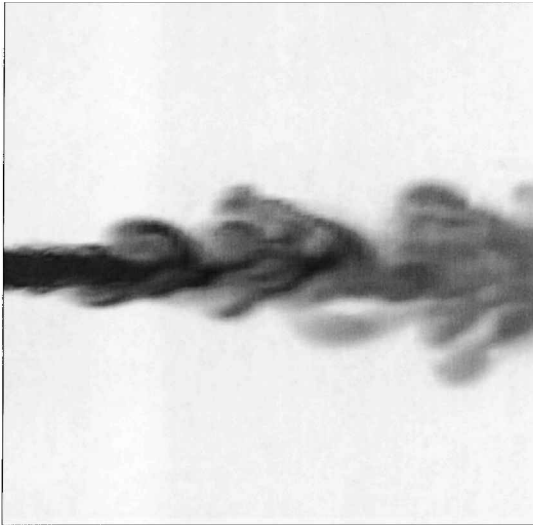


**Fig. 3** Instantaneous passive scalar contours produced by the dynamic mixed model on an  $xy$  plane,  $z = 8$ .

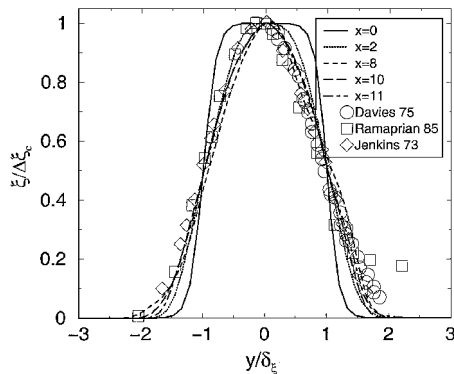


**Fig. 4** Dynamic mixed model: evolution of mean velocity profiles.

#### D. Evolution of the Mean Passive Scalar

Figure 4 shows mean profiles of the passive scalar at different streamwise stations obtained with the dynamic mixed model. Similar results are obtained with the dynamic Smagorinsky model. Similarity coordinates are used with the transverse  $y$  direction normalized by the jet scalar half-width  $\delta_\xi$ , whereas the passive scalar is normalized by the mean scalar difference at the centerline,  $\Delta\xi_c$ . At the inflow,  $x/h = 0.0$ , the scalar has a top-hat profile. At  $x = 2$ , the self-preserving profile is not yet established, and then, for  $x > 8$ , mean profiles tend to collapse. The mean passive scalar profiles compare well with experimental values.

The evolution of the mean centerline value of the scalar excess is presented in Fig. 5 together with the DNS results and experimental data for the centerline temperature decay in heated jets. Figure 6 shows the downstream growth of the scalar half-width. The evolution of the mean centerline value of the velocity excess and of the growth of the mean velocity are also presented on the same plot.

In the self-similar region, the mean scalar on the centerline varies as  $\xi_c \propto x^{-1/2}$  and can be fitted to  $(\xi_o/\xi_c)^2 = C_{1\xi}[(x/h) + C_{2\xi}]$ . The

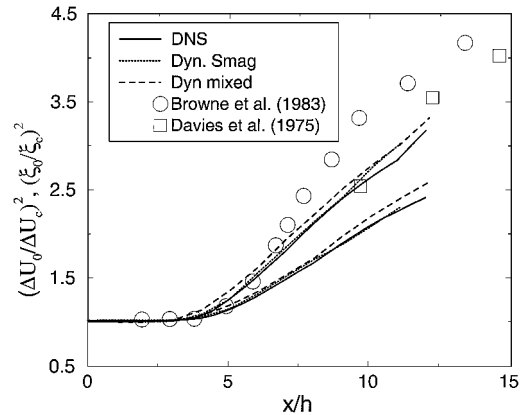


**Fig. 5** Decay of the mean scalar and centerline velocity excess on the jet centerline: upper curves and symbols correspond to mean scalar, lower curves correspond to mean velocity.

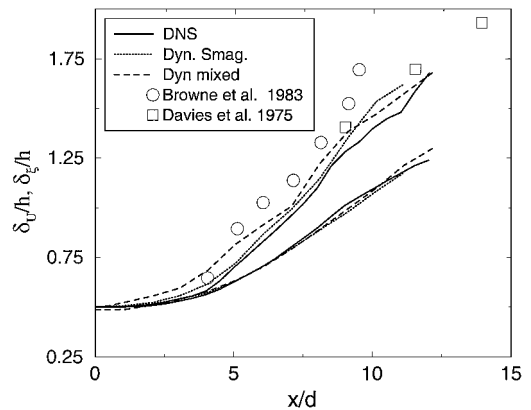


**Fig. 6** Downstream growth of the jet half-width based on the passive scalar and velocity: upper lines and symbols show  $\delta_\xi/h$ , and lower lines show  $\delta_u/h$ .

evolution of the scalar half-width corresponds to the functional form  $\delta_\xi/h = K_{1\xi}[(x/h) + K_{2\xi}]$ . Table 1 shows a comparison of those constants to experimental values for the temperature as well as DNS values. Both models give reasonable results compared with the DNS and the experimental results. For the scalar and for the velocity, the dynamic mixed model predicts slightly lower growth rates than the dynamic Smagorinsky model.

The spread rates and centerline decay rates for the scalar field are larger than those for the velocity field because the mixing of the scalar field occurs at a faster rate than for the velocity field, that is, the turbulent Prandtl number is less than unity.

#### E. Comparison of Higher Moments

The rms value of  $\xi$  deduced from the resolved-scale passive scalar field at the section  $x/h = 10$  is shown in Fig. 7. Both models are in good agreement with DNS results, but the dynamic Smagorinsky model is slightly closer to DNS.

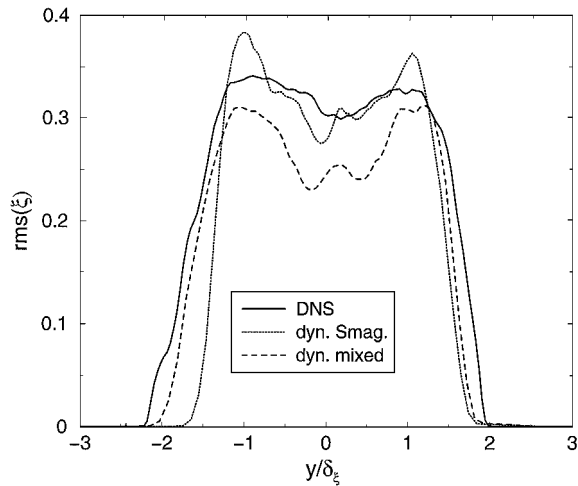


Fig. 7 Comparison of the streamwise turbulence intensity obtained with the different models at the section  $x/h = 10$ .

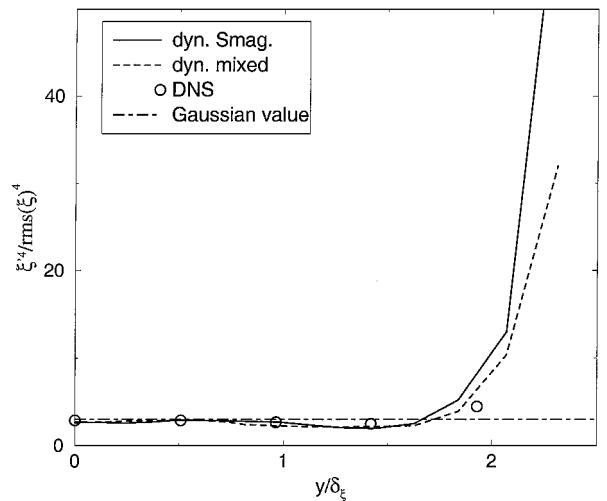


Fig. 9 Comparison of flatness obtained with different models at section  $x/h = 10$ .

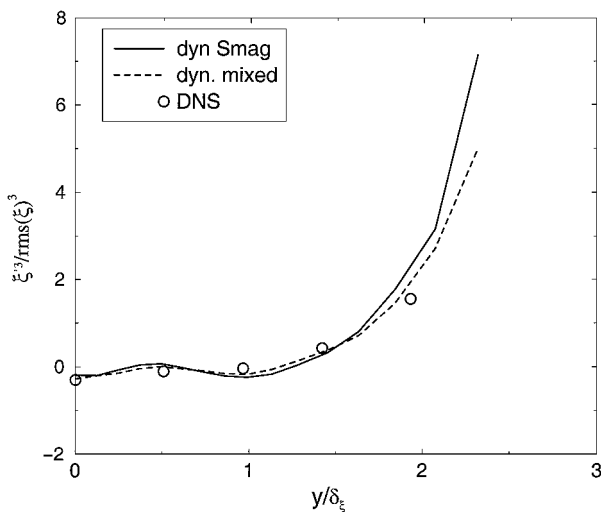


Fig. 8 Comparison of profiles of the skewness obtained with different models at section  $x/h = 10$ .

The third moment is given by

$$\langle \xi^3 \rangle = \int_{-\infty}^{\infty} (\xi - \langle \xi \rangle)^3 \text{PDF}(\xi) d\xi \quad (19)$$

and its normalized value, the skewness, is presented in Fig. 8. Here  $\langle \xi \rangle$  denotes the Reynolds average of the  $\xi$ . The probability density function (PDF) of the resolved-scale field is used for the calculation. The third moment represents transport by turbulence. The skewness is equal to the Gaussian value of zero at the center of the jet and then grows rapidly near the borders of the jet.

The fourth moment,

$$\langle \xi^4 \rangle = \int_{-\infty}^{\infty} (\xi - \langle \xi \rangle)^4 \text{PDF}(\xi) d\xi \quad (20)$$

is also computed using the resolved-scale PDF, and its normalized value, the flatness, at the same section is shown in Fig. 9. The flatness has an almost constant value, around the Gaussian value of 3 at the center of the jet and then increases rapidly near the jet borders. The flatness represents the spikiness of the turbulence.

The large departures of skewness and flatness near the jet edges from their Gaussian values is consistent with the external intermittency observed in experiments. Evidently, LES is able to capture external intermittency.

#### F. Dynamic Constant

Figure 10 presents profiles of the dynamic constant  $C_{d\xi}$  at various streamwise locations. The plots are presented for the dynamic

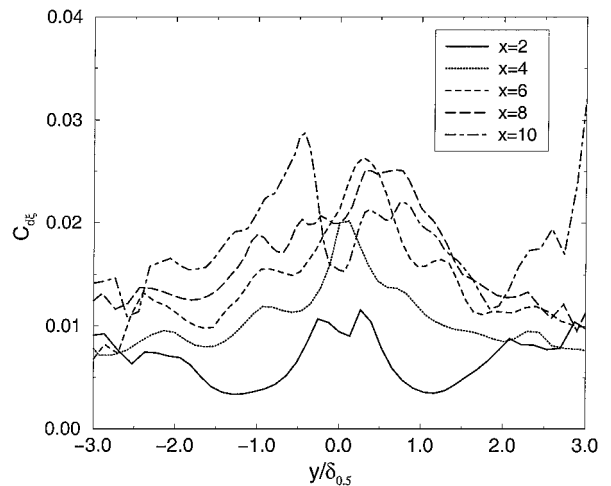


Fig. 10 Dynamic Smagorinsky model: downstream evolution of the dynamic constant.

Smagorinsky model, but similar results are obtained by the dynamic mixed model. The dynamic constant is low at  $x = 2$ , grows rapidly, and then shows small variations for  $x > 6$ . In the transverse direction, the dynamic constant is high in the center of the jet, where the turbulence intensity is large, showing that, with the dynamic procedure, the diffusivity adapts well to the flow.

Figure 11 presents, at one section ( $x/h = 10$ ), profiles of the dynamic constant  $C_{d\xi}$ , which appears in Eq. (7) for the subgrid scalar flux as well as the analogous coefficient  $C_{du}$ , in a dynamic eddy-viscosity model for the subgrid stress. The level of the constant is the same with the two models. The dynamic constants, especially for the scalar, tend to increase at the jet edges. However, as shown by Fig. 12, the subgrid transport coefficients at the jet edges remain small because the scalar and velocity gradients are small at those locations. The dynamic constant for the passive scalar is usually higher than the dynamic constant of the mean flow, consistent with the observation that the mixing of the passive scalar occurs at a faster rate than the velocity field. In the core of the jet, the ratio  $C_{du}/C_{d\xi}$  is approximately equal to 0.66, in good agreement with the ratio proposed by Horiuti<sup>7</sup> for the constant of the standard Smagorinsky model. Furthermore,  $C_{du}/C_{d\xi}$  is of the same order as the ratio  $C_{1u}/C_{1\xi}$  and  $K_{1u}/K_{1\xi}$ .

#### G. Evolution of the Passive Scalar PDFs

In the studies of mixing in turbulent shear layers, the PDF can be classified into marching, nonmarching, and tilted types.<sup>30</sup> In a marching PDF, the most probable value varies across the layer

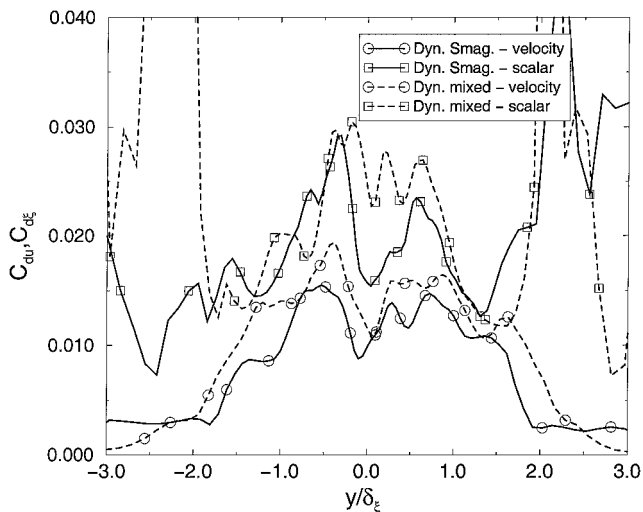


Fig. 11 Dynamic constants associated with scalar flux and momentum flux.

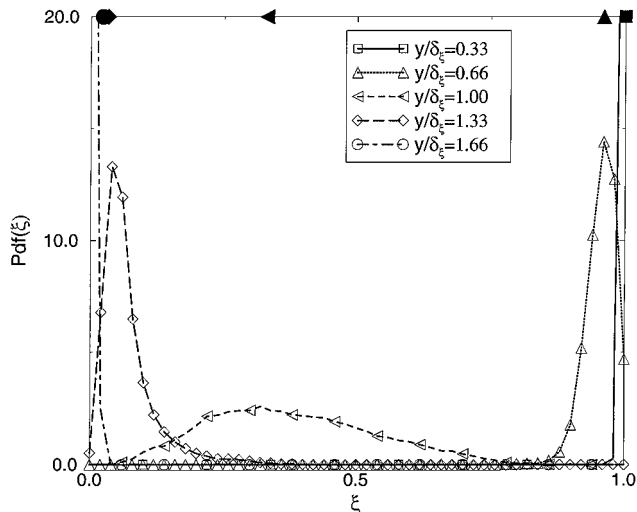


Fig. 13 Variation of PDF of the passive scalar across the jet at  $x/h = 1.0$ .

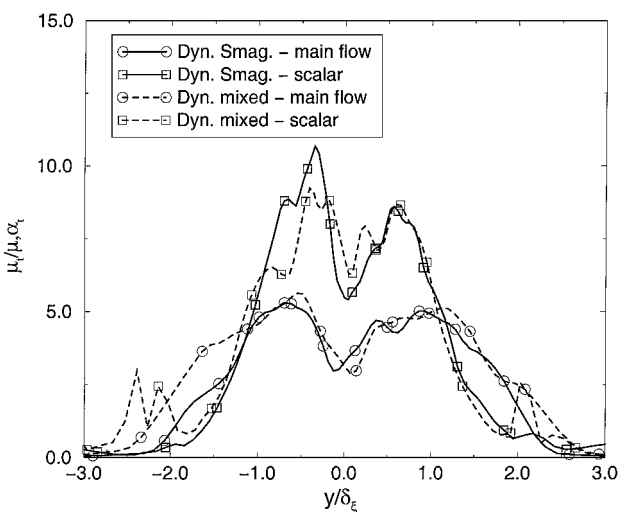


Fig. 12 Subgrid transport coefficients of both velocity and scalar associated with different models.

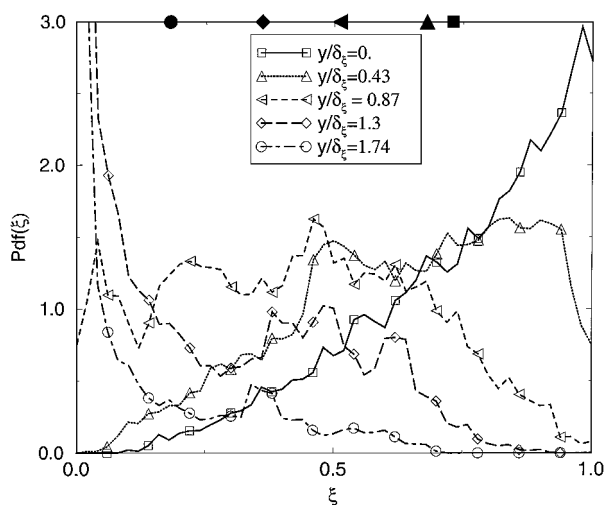


Fig. 14 Variation of PDF of the passive scalar across the jet at  $x/h = 7.0$ .

following the local mean value of the scalar. This type of PDF is characteristic of the classical notion of mixing dominated by the small scales of motion. In a nonmarching PDF, the most probable value remains at a constant location across the layer irrespective of the local mean value. This type of PDF characterizes mixing that is dominated by large-scale engulfing of pure fluid from the external streams. The tilted type is a hybrid of the two other types; the most probable value varies across the mixing region, but secondary peaks corresponding to unmixed fluid are present.

In the DNS,<sup>15</sup> immediately after the nozzle, the PDF has a marching behavior associated with the broadband inflow fluctuations and then after the vortex rollup and before the fully developed region becomes nonmarching. In the region of fully developed turbulence, the flow is again dominated at the center by small-scale structures, but, at the edges, large engulfing structures remain and double peaks in the PDF are present.

The goal is to see whether PDFs obtained with the filtered scalar field, without additional models for variation of the scalar around its filtered value at the subgrid level, are also able to reproduce the behavior of scalar PDFs obtained with DNS. The intensity of the inflow velocity fluctuations is the same as in the DNS with a maximum value of 5% at the shear layers. Results with the dynamic Smagorinsky model are shown for three streamwise locations,  $x/h = 1, 7$ , and  $11.5$ . DNS results from corresponding locations are given in the previous work<sup>15</sup> and are not shown here for brevity.

The PDFs are first presented at the streamwise station  $x/h = 1$ , for three lateral locations,  $0.33 < y/\delta_{\xi} < 1.66$ , ranging from the jet

centerline outward through the upper shear region (Fig. 13). At this section, the behavior of the jet is determined by the inflow conditions, and mixing is dominated by the effects of the broadband turbulence at the inflow. The filled symbols across the top of Fig. 13 give the mean values associated with the PDF drawn with the corresponding unfilled symbols. The peak in each PDF corresponds to the mean scalar value, and thus, the PDFs are of the pure marching type in agreement with the DNS. The width of the PDF is a measure of the mixing due to the velocity fluctuation. At  $y/\delta_{\xi} = 0.33$  and  $1.66$ , respectively, either pure jet fluid ( $\xi = 1$ ) or pure coflow fluid ( $\xi = 0$ ) is present. At  $y/\delta_{\xi} = 0.66$  and  $1.33$ , the PDF is wider, but the probability of having pure coflow or pure jet scalar is still high. At  $y/\delta_{\xi} = 1$ , the center of the upper shear layer, a broad range of scalar values is probable with peak at the mean scalar value. This station corresponds to where the intensity of the turbulence is the highest, and consequently, the mixing due to the velocity fluctuations is high. Compared to the DNS results, the overall behavior is the same, but in the LES the PDFs are wider and the peaks are shorter indicative of additional mixing due to subgrid fluctuations.

The PDFs at the downstream location  $x/h = 7$  and for five cross-stream stations are shown in Fig. 14. This location is at the end of the potential core and before the beginning of self-similarity. At  $y/\delta_{\xi} = 0$ , in the center of the jet, the probability of having pure coflow fluid is high. When the cross-stream location moves away from the jet centerline to  $y/\delta_{\xi} = 0.43, 0.87$ , and  $1.74$ , the mean scalar value (solid symbol at the top) progressively decreases. However, the peak of the PDF does not march along with the mean value

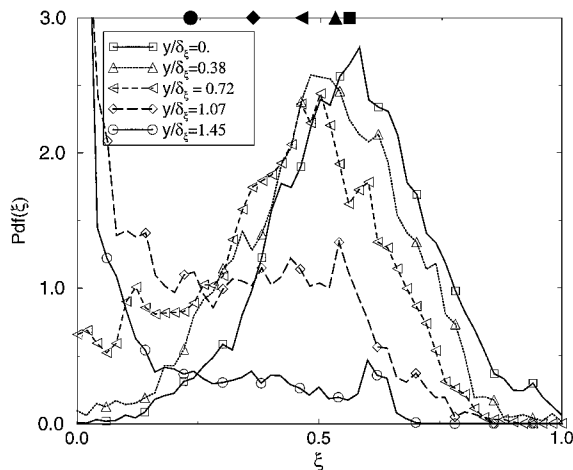


Fig. 15 Variation of PDF of the passive scalar across the jet at  $x/h = 11.5$ .

suggesting a nonmarching PDF. The results from DNS show the nonmarching behavior even more clearly. At  $y/\delta_\xi = 0$ , the probability of having pure jet fluid is much higher in the DNS than in the LES. At the station  $y/\delta_\xi = 0.87$ , the strong secondary peak, corresponding to pure jet that is present in the DNS, does not appear in the LES results. Thus, diffusivity, which is larger in the LES relative to the molecular value, reduces the presence of strong patches of unmixed jet fluid. This is an important difference between the PDF calculated using the filtered scalar field and the true PDF calculated using the DNS scalar field that leads to quantitative discrepancies between scalar moments obtained by LES with the true values. However, LES is able to qualitatively capture the nonmarching behavior of the PDFs at  $x/h = 7$  seen in the DNS.

Finally, the PDFs are presented at the section  $x/h = 11.5$  in the region with full-blown turbulence (Fig. 15). At  $y/\delta_\xi = 0$  and 1.07, there are single peaks close to the corresponding mean values, and the PDF exhibits a marching behavior. At  $y/\delta_\xi = 1.95$ , there is a strong peak corresponding to pure coflow fluid. At this station, similar to the DNS, the PDF at the jet centerline obtained with LES no longer shows a strong peak corresponding to pure jet fluid. Thus, the overall tilted PDF behavior at  $x/h = 11$  seen in the DNS is captured by the LES.

## V. Conclusions

A posteriori tests of subgrid models for the passive scalar evolution in a spatially developing jet are performed in the present work. Two different subgrid models are compared: the dynamic Smagorinsky model and the dynamic mixed model. Simulations are performed at the low Reynolds number of  $3 \times 10^3$  to compare mean and rms scalar evolution with corresponding DNS data. PDFs of the passive scalar are also computed because they provide complementary information about the flow and enable calculation of higher moments.

In visualizations of the passive scalar, the overall qualitative characteristics of scalar transport are well represented but without the small-scale details present in DNS. Both subgrid-scale models give reasonable results regarding the mean and rms scalar evolution compared with DNS and experimental results. However, from a priori tests, the dynamic mixed model is known to provide better representation of the subgrid stress tensor and this has been confirmed by our a posteriori simulations; therefore, the dynamic mixed model is recommended.

Higher scalar moments are also compared. The passive scalar has a Gaussian distribution at the jet centerline with the transport and intermittency sharply increasing near the jet borders.

The value of the dynamic constant is also investigated. The constant adapts well to the flow and is higher than the corresponding value for the velocity consistent with observations of higher mixing rates of a passive scalar compared to the velocity.

The PDF of the passive scalar obtained by LES at three sections is obtained and, without any correction for subgrid fluctuations, compared with the DNS results. Although the main characteristics of the PDF are well predicted, the LES results are broader than in DNS and the peaks smoother. The qualitative change from nonmarching to marching and tilted PDFs during the evolution of the scalar field is captured by LES.

## References

- Jenkins, P. E., and Goldschmidt, V. W., "Mean Temperature and Velocity in a Plane Turbulent Jet," *Journal of Fluids Engineering*, Vol. 95, No. 4, 1973, pp. 581–584.
- Davies, A. E., Keffer, J. F., and Baines, W. D., "Spread of a Heated Plane Turbulent Jet," *Physics of Fluids*, Vol. 18, No. 7, 1975, pp. 770–775.
- Browne, L. W. B., Antonia, R. A., Rajagopalan, S., and Chambers, A. J., "Interaction Region of a Two-Dimensional Turbulent Plane Jet in Still Air," *Structure of Complex Turbulent Shear Flow*, edited by R. Dumas and L. Fulachier, Springer, Berlin, 1983, pp. 411–419.
- Ramaprian, B. R., and Chandrasekhara, M. S., "LDA Measurements in Plane Turbulent Jets," *ASME Fluids Engineering*, Vol. 107, American Society of Mechanical Engineers, Fairfield, NJ, 1985, pp. 264–271.
- Lesieur, M., and Metais, O., "New Trends in Large-Eddy Simulations of Turbulence," *Annual Review of Fluid Mechanics*, Vol. 28, 1996, pp. 45–82.
- Moin, P., "Progress in Large Eddy Simulation of Turbulent Flows," AIAA Paper 97-0749, 1997.
- Horiuti, K., "Assessment of Two-Equation Models of Turbulent Passive Scalar Diffusion in Channel Flow," *Journal of Fluid Mechanics*, Vol. 238, 1992, pp. 405–433.
- Moin, P., Squires, K., Cabot, W., and Lee, S., "A Dynamic Subgrid-Scale Model for Compressible Turbulence and Scalar Transport," *Physics of Fluids A*, Vol. 3, No. 11, 1991, pp. 2746–2757.
- Akselvoll, K., and Moin, P., "Large-Eddy Simulation of Turbulent Confined Coannular Jets," *Journal of Fluid Mechanics*, Vol. 315, 1996, pp. 387–411.
- Vreman, B., Geurts, B., and Kuerten, H., "Comparison of Numerical Schemes in Large Eddy Simulation of the Temporal Mixing Layer," *International Journal for Numerical Methods in Methods Fluids*, Vol. 22, No. 4, 1996, pp. 297–311.
- Pullin, D. I., "A Vortex-Based Model for the Subgrid Flux of a Passive Scalar," *Physics of Fluids*, Vol. 12, No. 9, 2000, pp. 2311–2319.
- Cook, A. W., and Riley, J. J., "A Subgrid Model for Equilibrium Chemistry in Turbulent Flows," *Physics of Fluids*, Vol. 6, 1994, pp. 2868–2870.
- Pierce, C. D., and Moin, P., "A Dynamic Model for Subgrid-Scale Variance and Dissipation Rate of a Conserved Scalar," *Physics of Fluids*, Vol. 10, No. 12, 1998, pp. 3041–3044.
- Pantano, C., and Sarkar, S., "A Subgrid Model for Nonlinear Functions of a Scalar," *Physics of Fluids* (to be published).
- Stanley, S., and Sarkar, S., "Direct Simulation of the Flow and Scalar Evolution in a Turbulent Plane Jet," *Journal of Fluid Mechanics* (to be published).
- Le Ribault, C., Sarkar, S., and Stanley, S., "Large Eddy Simulation of a Plane Jet," *Physics of Fluids*, Vol. 11, No. 10, 1999, pp. 3069–3083.
- Libby, P. A., and William, F. A., "Turbulent Reacting Flows," *Topics in Applied Physics*, Vol. 44, Springer-Verlag, New York, 1980.
- Smagorinsky, J., "General Circulation Experiments with the Primitive Equations," *Monthly Weather Review*, Vol. 91, No. 3, 1963, pp. 99–164.
- Germano, M., Piomelli, U., Moin, P., and Cabot, W. H., "A Dynamic Subgrid-Scale Eddy Viscosity Model," *Physics of Fluids A*, Vol. 3, No. 7, 1991, pp. 1760–1765.
- Lele, S. K., "Compact Finite Difference Schemes with Spectral Like Resolution," *Journal of Computational Physics*, Vol. 103, No. 1, 1992, pp. 16–42.
- Carpenter, M. H., Gottlieb, D., and Abarbanel, S., "Stability of Numerical Boundary Treatments for Compact High-Order Finite-Difference Schemes," *Journal of Computational Physics*, Vol. 108, No. 2, 1993, pp. 272–295.
- Zalesak, S. T., "Fully Multidimensional Flux-Corrected Transport Algorithms for Fluids," *Journal of Computational Physics*, Vol. 31, No. 3, 1979, pp. 335–362.
- Thompson, K. W., "Time Dependent Boundary Conditions for Hyperbolic Systems," *Journal of Computational Physics*, Vol. 68, No. 1, 1987, pp. 1–24.
- Giles, M. B., "Nonreflecting Boundary Conditions for Euler Equation Calculations," *AIAA Journal*, Vol. 28, No. 12, 1990, pp. 2050–2058.

<sup>25</sup>Rudy, D. H., and Strikwerda, J. C., "A Non-Reflecting Outflow Boundary Condition for Subsonic Navier–Stokes Calculations," *Journal of Computational Physics*, Vol. 36, No. 1, 1980, pp. 55–70.

<sup>26</sup>Hu, F. Q., "On Absorbing Boundary Conditions for Linearized Euler Equations by a Perfectly Matched Layer," *Journal of Computational Physics*, Vol. 129, No. 1, 1996, pp. 201–219.

<sup>27</sup>Vreman, B., "Direct and Large Eddy Simulation of the Compressible Turbulent Mixing Layer," Ph.D. Dissertation, Dept. of Applied Mathematics, Univ. of Twente, Twente, The Netherlands, 1995.

<sup>28</sup>Salvetti, M. V., and Beaux, F., "The Effect of the Numerical Scheme on the Subgrid Scale Term in Large-Eddy Simulation," *Physics of Fluids A*,

Vol. 10, No. 11, 1998, pp. 3020–3022.

<sup>29</sup>Kravchenko, A. G., and Moin, P., "On the Effect of Numerical Errors in Large Eddy Simulations of Turbulent Flows," *Journal of Computational Physics*, Vol. 131, No. 2, 1997, pp. 310–322.

<sup>30</sup>Karasso, P. S., and Mungal, M. G., "Scalar Mixing and Reaction in Plane Liquid Shear Layers," *Journal of Fluid Mechanics*, Vol. 323, 1996, pp. 23–63.

K. Kailasanath  
Associate Editor